Electrical conduction processes in aluminum: Defects and phonons

Kashi N. Subedi, Keerti Kappagantula, Frank Kraft, Aditya Nittala, and David A. Drabold

Phys. Rev. B **105**, 104114 — Published 31 March 2022

DOI: 10.1103/PhysRevB.105.104114

Electrical conduction processes in aluminum: defects and phonons

Kashi N. Subedi,[1,*] Keerti Kappagantula,[2] Frank Kraft,[3] Aditya Nittala,[2] and David A. Drabold[1,†]

[1]*Department of Physics and Astronomy, Nanoscale and Quantum Phenomena Institute (NQPI), Ohio University, Athens, Ohio 45701, USA*
[2]*Pacific Northwest National Laboratory, Richland, WA 99352, USA*
[3]*MetalKraft Technologies, LLC, Albany, OH 45710, USA*

(Dated: March 14, 2022)

It is well known that disorder (structural or thermal) induces electronic scattering processes which determine the resistivity of crystalline metals. In this paper, we employ a novel variant of the Kubo-Greenwood formula to compute the space projected conductivity and study the atomistic details of conduction in models of crystalline aluminum within the framework of density functional theory. We consider point and extended lattice defects and show with spatial detail *how* the defect locally affects conduction. We simulate thermal disorder and determine how the disorder affects the conductivity in real space and reveal the spatial nature of thermal fluctuations. Furthermore, we show that well below the Debye temperature, a classical thermal molecular dynamics simulation reproduces the form of temperature dependent conductivity predicted by the Bloch Grüneisen formula.

I. INTRODUCTION

Transport theory in metals is one of the classic stories of science. The Boltzmann transport equation [1, 2] estimates the dynamics of the electronic distribution function taking into account external fields and the collision processes. With the development of quantum mechanics, Sommerfeld introduced Fermi-Dirac statistics and a free electron model [3]. Houston [4], and Frenkel and Mirolubow [5] discussed scattering of electron waves by crystals, but it was Felix Bloch who established the basis of modern theory of metallic electrons [6]. The quantum mechanical theories of transport in liquid metals appeared in the 1950s [7], and were a substantial development over earlier models.

From a different point of view – the statistical mechanics of linear response – Kubo explored the linear response of a material to an external AC electric field [8]. The resulting expression for the electrical conductivity, further approximated within a single particle picture of the electronic structure, is known as the Kubo-Greenwood formula (KGF). This was later generalized as the "Fluctuation-Dissipation theorem" that mathematically connects dissipative process with fluctuations for systems near equilibrium [9]. The KGF has become a widely used method to compute electronic conductivity. It has been implemented in the Green's function formalism [10, 11], density functional theory (DFT) [12–19] with great success. An *ab initio* estimate of the temperature dependence of conductivity on amorphous solids has also been obtained from KGF [15]. Where metals are concerned, the KGF has been employed to compute conductivity of highly disordered or liquid metals [17, 18]. To our knowledge, *no attempt* has been made to compute the temperature dependence of the conductivity in a low temperature range that represents a weakly disordered phase of the metal. It is known from experiments that the resistivity of simple metals closely follow the Bloch Grüneisen T^5 law at low temperatures [20] analogous to Debye's form for the specific heat.

DFT methods have been used to study lattice defects in metals. There have been studies ranging from structural stability of defects [21] to charge transport [22]. However, a full atomistic grasp of conduction with defects in metals is lacking. It is of interest to know quantitatively *how* the conduction is spatially affected by such defects. Recently, we have devised a method to exploit the KGF in a novel way – to determine the conduction active elements of materials exploiting a spatial decomposition of the KGF. We have dubbed this the "space-projected conductivity" (SPC). We have applied the method to several problems in mixed semiconducting systems (as for example conducting bridge computer memory materials [23–26]). These computations identify conduction pathways in heterogeneous materials and provide useful information for problems of material design. We also reported conduction fluctuations in liquid silicon [27]. Here, we extend this type of analysis to Face Centered Cubic (FCC) aluminum (Al), with defects and thermal disorder. In one of our earlier works, we observed uniform spatial distribution of conduction in crystalline Al [27]. We also showed that the spectrum of conduction eigenvalues for this metal possesses an extended tail that is absent in semiconductor/insulating systems.

In this paper, we study two different processes that affect the conductivity of metals. First, we discuss thermal disorder using a quantum molecular dynamics (QMD) approach at a chosen temperature, and use KGF method to compute conductivity. We show that the KGF correctly predicts the temperature dependence of conductivity. Second, we discuss the role of lattice defects on conduction of the metal. We show that reduction of conduction due to defects is substantial and produce estimates for the spatial range of "conduction damage" induced by these defects. For this, we consider two different types of defects, namely vacancies, and the grain boundaries (GBs). For vacancies, we keep our analysis

* ks173214@ohio.edu
† drabold@ohio.edu

simple by considering a single and a di-vacancy in a single crystal. For GBs, we consider two symmetric tilt grain boundaries models and visualize conduction pathways in the vicinity of these GBs. To study the conduction near the vacancies and GBs, we utilize our recently proposed method to project conductivity onto real space [23].

The rest of this paper is organized as follows. In section II , we discuss details about models and the computaional methodologies employed in this paper. In section III, we provide results on electronic conduction processes for different kinds of defects present in aluminum. We summarize our findings in section IV.

II. MODELS AND METHODS

A. Simulation of thermal disorder

For estimating the effects of thermal disorder on conduction, we created a 4 $\times$ 4 $\times$ 4 structure from the FCC primitive cell to form a supercell with 256 atoms. To model thermal disorder, we simply average the KGF over a constant temperature MD simulation. For any MD snapshot, the thermal disorder induces inhomogeneous conduction in space, as gauged by the SPC. Such a procedure is obviously suspect for $T < \Theta_D$ for Θ_D being the Debye temperature, and must fail as $T \to 0$ as the classical dynamics freeze out. It is of interest how this crude approximation is reasonable to a temperature lower than Θ_D in a sense that the resistivity given by experiment or the Bloch-Grüneisen formula is well reproduced.

We implemented *ab initio* molecular dynamics simulations (AIMD) to obtain representative models at different temperatures. Snapshots of the Al crystal at a selected temperature T was obtained by equilibrating the cell and sampling steps near the end of a 2 picoseconds (ps) run. A time step of 1.5 femtoseconds (fs) was used, and the temperature was controlled by a Nosé-Hoover thermostat [28–30]. The last configuration from each temperature was used as a starting configuration for the succeeding temperature. For each temperature, the last ten configurations at an interval of 10 steps (15 fs) were chosen for the conductivity calculations. Static calculations were performed at 4 **k**-points sampled on the first Brillouin zone using Monkhorst-Pack scheme.

B. Defects

Vacancies: For this case, we constructed a 5 $\times$ 5 $\times$ 5 structure from the FCC primitive cell, yielding a cubic supercell 20.25 Å on a side, consisting of 500 atoms. Single and di-vacancies were then created by removing atom/s from the supercell. For these larger models with vacancies, static calculations were performed at Γ point.

Grain boundaries: We also considered a few possible GBs. GBs are often described by the nomenclature Σ, tilt/twist angles, symmetric/asymmetric GB, crystallographic directions, and specification of GB planes. The term Σ corresponds to the reciprocal of the density of coincident site lattice (CSL). For example, Σ5 has 1/5 of the atoms in the CSL. The tilt boundaries are often described by a shared tilt axis that lies within the grain boundary plane, for e.g., $\langle 1\ 0\ 0 \rangle$, and either one (symmetric) or two (asymmetric) planes. For further information on the crystallography of the GBs and the CSL, the reader is referred to references [31, 32]. We created two symmetric grain boundary models namely Σ5 $\{$-3 1 0$\}$ $\langle 1\ 0\ 0 \rangle$ and Σ13 $\{0$ -2 3$\}$ $\langle 1\ 0\ 0 \rangle$. The misorientation angles for these grain boundary models are 36.87° and 22.62° respectively. In these models, there are two GBs, one at the middle of the supercell, and the other at the interface on the boundaries parallel to the middle GB because of the periodic boundary conditions. The distance between the middle and interface GBs were kept at a distance of at least 25 Å to minimize the interactions between these GBs. This resulted in orthorhombic supercells with 936 and 816 atoms respectively. 50 initial structures for each GBs were obtained by translating atoms slightly along the GB plane. The minimum distance between the Al atoms at GB was no less than 2.56 Å. For these 50 structures, zero pressure relaxations were done separately using the conjugate gradient (CG) method, and the structure with minimum energy was chosen. Since the cells were large, relaxations were performed with LAMMPS using the embedded-atom method (EAM) [33]. The force acting on each atom was computed using VASP for these relaxed models which were relatively small (0.01 eV/Å). Static calculations were then performed using VASP to obtain the information for conductivity calculations.

C. Energy functionals and electron-ion interactions

The AIMD calculations were performed employing the Viennna *Ab-initio* Simulation Package (VASP) [34]. A plane-wave basis set was used with kinetic energy cutoff of 250 eV. For static calculations, a larger cutoff of 320 eV was used. We used projected augmented wave (PAW) potentials [35] to account for the ion-electron interaction, and the generalized gradient approximation (GGA) of Perdew-Burke-Ernzerhof (PBE) [36] as the exchange-correlation functional.

D. Space Projected Conductivity

In this section, we summarize a method to project electronic conductivity onto real-space grids by exploiting the Kubo-Greenwood formula (KGF) [8, 37]. The average conductivity from the diagonal elements of the conductivity tensor for any

frequency ω can be expressed as:

$$\sigma(\omega) = \frac{2\pi e^2}{3m^2\Omega\omega} \sum_{\mathbf{k}} w_{\mathbf{k}} \sum_{i,j} \sum_{\alpha} \Big(f(\epsilon_{i,\mathbf{k}}) - f(\epsilon_{j,\mathbf{k}})\Big) \\ |\langle\psi_{j,\mathbf{k}}|p^{\alpha}|\psi_{i,\mathbf{k}}\rangle|^2 \delta(\epsilon_{j,\mathbf{k}} - \epsilon_{i,\mathbf{k}} - \hbar\omega) \quad (1)$$

In Eq. (1), *e* and *m* represent the charge and mass of the electron respectively. Ω is the volume of the supercell, and ω the frequency. Here, $w_{\mathbf{k}}$ are the **k**-point integration weights. $\psi_{i,\mathbf{k}}$ is the non-spin polarized Kohn-Sham orbital associated with energy $\epsilon_{i,\mathbf{k}}$ and $f(\epsilon_{i,\mathbf{k}})$ denotes the Fermi-Dirac weight. p^{α} is the momentum operator along each Cartesian direction α. Let us rewrite Eq. (1) with terms involving energies (bands) and spatial part α separately

$$\sigma = \sum_{\mathbf{k}} w_{\mathbf{k}} \sum_{i,j,\alpha} g_{ij,\mathbf{k}} \, |\langle\psi_{j,\mathbf{k}}|p^{\alpha}|\psi_{i,\mathbf{k}}\rangle|^2 \quad (2)$$

where

$$g_{ij,\mathbf{k}} = \frac{2\pi e^2}{3m^2\Omega\omega} \Big(f(\epsilon_{i,\mathbf{k}}) - f(\epsilon_{j,\mathbf{k}})\Big) \delta(\epsilon_{j,\mathbf{k}} - \epsilon_{i,\mathbf{k}} - \hbar\omega).$$

To project the conductivity onto real-space, Eq. (2) is written in the position representation with x and x' as dummy variables:

$$\sigma = \sum_{\mathbf{k},i,j,\alpha} w_{\mathbf{k}} \, g_{ij,\mathbf{k}} \int d^3x \int d^3x' \Big(\psi^*_{j,\mathbf{k}}(x) p^{\alpha} \psi_{i,\mathbf{k}}(x)\Big) \\ \Big(\psi^*_{j,\mathbf{k}}(x') p^{\alpha} \psi_{i,\mathbf{k}}(x')\Big)^* \quad (3)$$

If we define complex valued functions $\xi^{\alpha}_{ji,\mathbf{k}}(x) = \psi^*_{j,\mathbf{k}}(x) p^{\alpha} \psi_{i,\mathbf{k}}(x)$ on a real space grid (call the grid points *x*) with uniform spacing of width *h* in three dimensions, then we can approximate the integrals as a sum on the grids. Thus, Eq. (3) can be written as:

$$\sigma \approx h^6 \sum_{x,x'} \sum_{\mathbf{k},i,j,\alpha} w_{\mathbf{k}} \, g_{ij,\mathbf{k}} \, \xi^{\alpha}_{ji,\mathbf{k}}(x) \Big(\xi^{\alpha}_{ji,\mathbf{k}}(x')\Big)^* \quad (4)$$

In the preceding equation, the approximation becomes exact as $h \to 0$. If we define a Hermitian, positive semi-definite matrix:

$$\Gamma(x,x') = h^6 \sum_{\mathbf{k},i,j,\alpha} w_{\mathbf{k}} \, g_{ij,\mathbf{k}} \, \xi^{\alpha}_{ji,\mathbf{k}}(x) \Big(\xi^{\alpha}_{ji,\mathbf{k}}(x')\Big)^* \quad (5)$$

we can spatially decompose the conductivity at each grid point as $\zeta(x) = |\sum_{x'} \Gamma(x,x')|$. $\zeta(x)$ contains vital information about the conduction-active parts of the system. We showed elsewhere that the eigenvectors of Γ provide a convenient and often compact description of electronic conduction [27].

To implement the method, we used VASP and associated Kohn-Sham orbitals $\psi_{i,\mathbf{k}}$, nevertheless, the method is suitable for any appropriate basis sets. A grid-spacing in the range of $\approx$ 0.3-0.5 Å was used. We then projected wavefunction corresponding to each band onto a grid point [38]. ξ^{α}_{ji} are obtained using a centered finite-difference method to compute the gradient of ψ_i with respect to direction α. We have averaged over Cartesian indices α. We used an electronic temperature of T = 1000 K in the Fermi-Dirac distribution. The δ function in Eq. (1) is approximated by Gaussian distribution of different widths in the range 0.005-0.04 eV, which we discuss in more detail below. The impact on the conductivity due to different factors such as smearing width, number of atoms, smearing temperature, energy-cutoff for the finite sized cells are discussed in references [18, 19, 39].

III. RESULTS AND DISCUSSIONS

A. Temperature dependence of the conductivity

In this section, we study the effects of thermal disorder on conductivity. We first present the results of thermally averaging the KGF to estimate the T-dependence of the conductivity, and then briefly discuss the spatial distribution of conduction at two different temperatures: one at room temperature and the other near the melting point.

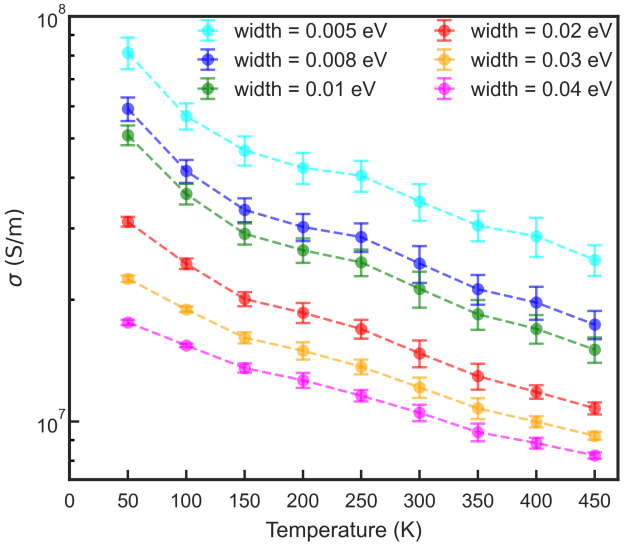

Figure 1. Electronic conductivity (logarithmic scale) computed using Kubo-Greenwood formula at different temperatures. The bars correspond to standard deviation from the mean conductivity averaged from last ten snapshots that are 15 fs apart at the end of 2 ps MD. "width" in legends are the values of smearing widths used in Gaussian distribution function to approximate the δ function in Eq. 1

Figure 1 shows the thermally averaged conductivity computed using KGF from last ten snapshots of 2 ps annealing. From Fig. 1, we see that the value of the conductivity is sensitive to the choice of smearing width, nevertheless, the shape of the conductivity as a function of T is not much affected (though the value of the conductivity varies by a factor of $\approx$ 4 over the range of widths selected). In our previous work, we have observed conductivities within a factor of

10 (or better). This is not surprising in view of the sensitivity of the conductivity to cell size effects, **k**-points, intrinsic limitations of the KGF etc [15, 40]. One of the well known challenges of KGF calculations is handling the δ function in Eq. 1. For a supercell, the number of states near the Fermi level (E_F) scales with the number of atoms. For small cells and defective seimconductors (for example), there will be inadequate sampling of the relevant states, so that some strategy is required to mimic the thermodynamic limit. The most obvious expedient is to simply broaden the δ function to include more states near the E_F. On the other hand, for metals like Al, there are large number of bands near the E_F even for our small supercells. For the chosen models in our calculations, we observe that splitting of these states lie within $\approx$ 0.01-0.03 eV and is affected by the temperature. The conductivity with smearing widths of 0.01 eV and smaller is mostly attributed to intra-band transitions and is closely analogous to Drude conductivity. Since, the conductivity follows almost the same trend for the selected smearing widths, we fitted the resistivity derived from the KGF with Bloch Grüneisen formula [41] for smearing width 0.02 eV that includes the contribution from both intra and inter-band transitions. The Bloch Grüneisen formula is expressed as:

$$\rho(T) = \rho_0 + A(\frac{T}{\Theta_D})^5 \int_0^{\Theta_D/T} \frac{x^5}{(e^x-1)(1-e^{-x})} dx \quad (6)$$

where ρ_0 is the residual resistivity and is independent of temperature, A is the prefactor of Bloch-Grüneisen formula and is proportional to the electron-phonon coupling constant, Θ_D is the Debye temperature of the metal.

The resistivity using KGF and the fit using Bloch Grüneisen formula at selected temperatures are shown in Fig. 2. The calculated and fitted values of resistivity are represented by solid blue circles and solid red stars respectively. The orange dashed line represents the fit using Bloch Grüneisen formula for every 10 K apart to aid visualization. The scattered green solid diamonds correspond to the experimental data. From Fig. 2, we see that the calculated values differ by a factor of $\approx$ 2.4 from experiment. One can see that the resistivity provides a good fit to Eq. 6, and is proportional to T^5 law. For larger supercells that have relatively narrower splitting of electronic states near E_F, one has flexibility of using smaller broadening width that provides better agreement with the experiment. For the current models, we find that the smearing width of 0.005 eV closely agrees with the experiment. For T $<$ 50 K, the method fails as the quantum nature of the phonon dominates.

As an illustration to simulate the effect of thermal disorder on conduction, we computed the SPC from two different models, one at 300 K (room temperature) and other at 900 K (near melting point). Figure 3 displays SPC as isourface colormap of inverted rainbow spectrum (ROYGBIV) obtained from those models. The top and bottom sub-plots correspond to 300 K and 900 K respectively. From Fig. 3, it is apparent that there exists a higher reduction of conduction at 900 K compared with 300 K. At room temperature, the conduction still appears uniform (deep blue and violet color on the top sub-

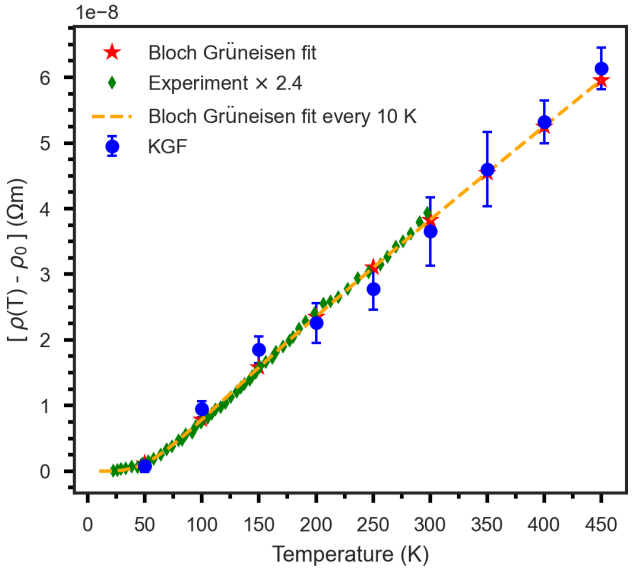

Figure 2. Resistivity derived from the KGF (smearing width 0.02 eV) calculated at different temperatures (blue solid circles), and the fitted values using Eq. 6 (red solid stars). The blue bars correspond to standard deviation from the mean resistivity that is computed from the KGF. The orange dashed line is added as a guide for visualization that passes along the fitted values. The experimental data is shown by green solid diamonds taken from reference [42]. There is a factor of 2.4 between the calculated and the experimental values.

plot in Fig. 3) whereas near the boiling point, the conduction is quite random. We see relatively more conduction deficit regions (shown by orange/yellow colored regions in the bottom sub-plot in Fig. 3) compared with room temperature.

B. Spatial distribution of conduction in Al with vacancies

In this sub-section, we discuss the spatial distribution of conduction in aluminum (ca. 500 atoms model) with single and di-vacancies. For this, we computed space-projected conductivity from both types of vacancies as discussed in Section II D, and visualized it along a few crystallographic planes. We also discuss the directional dependence of the conductivity along those chosen crystallographic planes.

1. *Single vacancy*

a. 010 plane: Figure 4a is a gray-scale plot of conductivity projected on the grids closest to 010 plane of the supercell containing the vacancy. From Fig. 4a, it is apparent that the primary effect is very local, and the effect decays on moving away from the vacancy. The distance over which the vacancy produces significant effect to the conductivity can be termed "reduction range". This distance may also be viewed as "recovery length" over which the conduction is likely to be recovered that is affected by the defect. For consistency, we

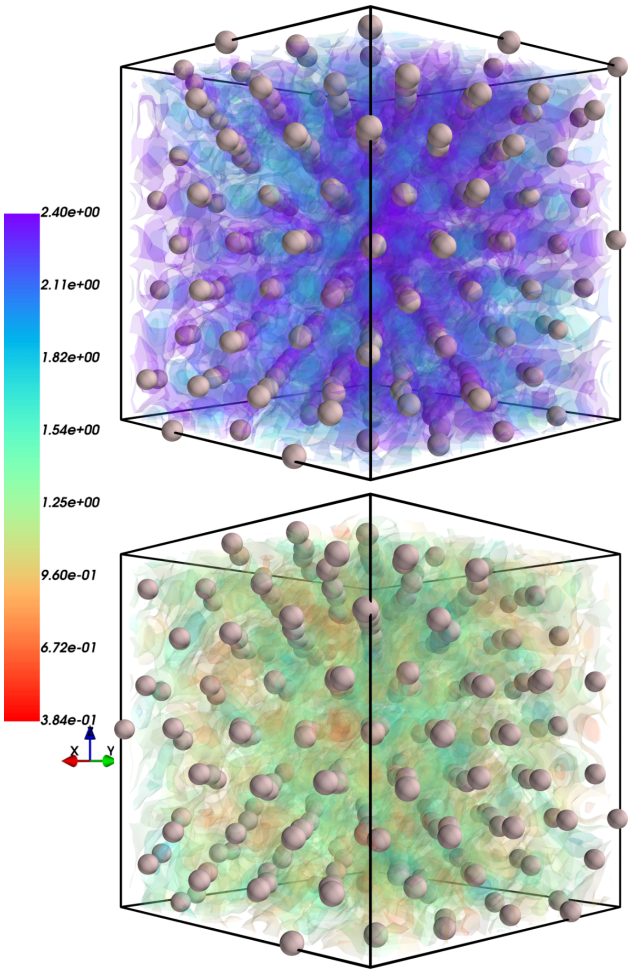

Figure 3. SPC (ζ) projected on grids as color-map plot (units in S/cm) corresponding to different temperatures. Top: room temperature (300 K) and bottom: near melting point (900 K). The inverted rainbow colorbar shows the magnitude of SPC scaled with maximum value at 900 K. The gray spheres represent Al atoms.

pick the latter in the rest of the paper. Figure 4d displays the behavior of SPC away from the vacancy at different angles on 010 plane (θ = 0°). It can be seen that there is slight anisotropy around the vacancy. The recovery length along the axes (ϕ = 0°, 90°) is ≈ 2.96 Å. Similarly, along other angles with ϕ = 45° and complementary angles (ϕ = 26.56°, 63.44°), the conduction recovers at a distance of ≈ 2.80 Å and 2.76 Å respectively. The recovery length along the studied directions is close to first nearest neighbor distance (≈ 2.86 Å), and therefore the effect of the vacancy can be considered local as visually observed in Fig. 4a.

b. 011 plane: Figure 4b displays the SPC projected on 011 plane as a gray-scale 2D plot. On this plane, the effect of vacancy to the conduction spans from local to intermediate range, and has relatively more anisotropy compared with the 010 plane. Figure 4e shows the variation of SPC with distance along different directions on this plane. The conduction along the direction shown by yellow lines in Fig. 4 (b & e) with (θ, ϕ = 90°, 135°) recovers at a distance of ≈ 4.1 Å. The recovery length along the direction shown by green lines in Fig. 4 (b & e) with (θ, ϕ) = (135°, 125°), is the longest and is ≈ 6.0 Å. We see similar recovery length along (θ, ϕ) = (45°, 125°), and is shown by orange lines in Figs. 4 (b & e).

c. 111 plane: Fig. 4c is a gray-scale plot of SPC projected onto the 111 plane. The effect of the vacancy on this plane also ranges from local to intermediate range as observed on 011 plane. Figure 4f shows the variation of SPC with distance along different directions. The recovery length on this plane also varies with direction. The recovery length along the directions pointing towards left and bottom left (blue and red colored lines in Fig. 4c) with (θ, ϕ) = ((315°, 90°) and (0°, 135°)) are short and are ≈ 3.5 Å. The recovery length along the directions shown by magenta and green colored lines in the same figure with (θ, ϕ) = (45°, 145°) and (124°, 106°) is ≈ 6.0 Å.

2. *Di-vacancies*

a. 010 plane: Figure 5a illustrates the SPC projected on the grids closest to the 010 plane with two adjacent vacancies. The spatial distribution of conduction around each vacancy towards opposite end of either vacancies is similar to the distribution around single vacancy (refer Fig. 4a). The distribution of conduction is dumb-bell shaped. Figure 5d shows the distribution of SPC from the grid closest to the center of the two adjacent vacancies along different directions. From Fig. 5d, we see that the distribution is highly anisotropic in nature. Along the z-axis (θ, ϕ = 0°, 0°), the reduction recovers from the center joining the vacancy at a distance of ≈ 6.9 Å. Along the positive x-axis (θ, ϕ = 0°, 90°), the the recovery length from the center is ≈ 9.3 Å, and from the left vacancy is ≈ 6.9 Å. Along the direction with ϕ = 27°, the recovery length is ≈ 7.7 Å. Along other directions with ϕ = 45° and 135°, the recovery length is ≈ 7.6 Å. The reduction caused by the di-vacancy is intermediate, and the recovery length is more than twice caused by the single vacancy projected on same plane.

b. 011 plane: Figure 5b displays the SPC projected on the grids closest to 011 plane. One can see that the effect of the vacancies is more than local range along all directions on the plane. The distribution of the conduction towards the opposite end is similar to that of 010 plane, however, along the other directions, the distribution is different. Figure 5e shows the distribution of SPC from the grid closest to the center of the two adjacent vacancies along different directions on this plane. From Fig. 5e, it is clear that there exists a high degree of anisotropy similar to what was observed in 010 plane. We find the variation in reduction along different directions. The recovery lengths are from ≈7 .0 Å to ≈ 9.3 Å. In other words, the affect of the vacancy is mostly either intermediate or long-ranged in nature. Along directions with (θ, ϕ = 27°,114°), (45°,125°), the recovery length is ≈ 8.6 Å. Along the direction pointing downwards (yellow colored line Fig. 5b) with (θ, ϕ = 90°, 135°), the length is ≈ 7.0 Å.

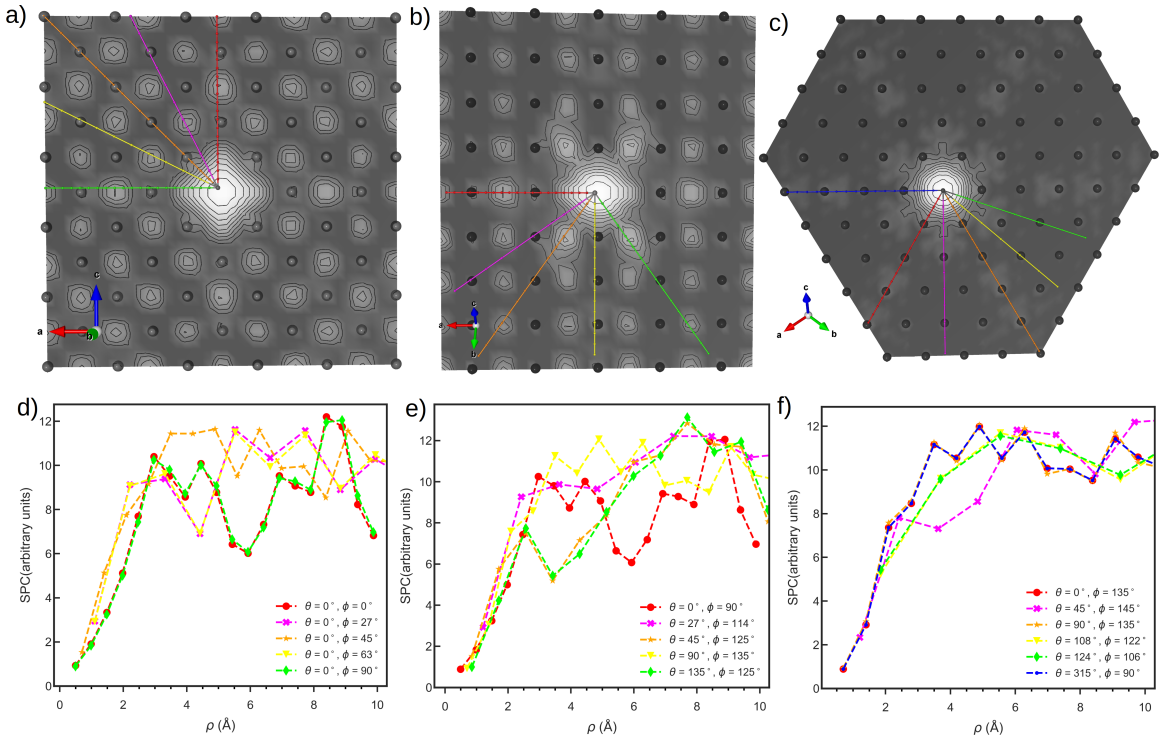

Figure 4. a), b), c): Conductivity projected on grids closest to crystallographic planes 010, 011 and 111 containing vacancy as a 2D gray scale plot. The magnitude of conductivity increases from white to black. The colored lines with small spheres are just for guide to an eye representing different directions from the vacancy. d), e), f): Variation of conductivity with distance from the grid closest to the vacancy along different directions on planes 010, 011 and 111 respectively. θ and ϕ refer to the polar and azimuthal angles respectively. Colors of legends in d), e), f) match with the lines shown in a), b), c) respectively.

c. 111 plane: Figure 5c shows the SPC on the grids that are closest to the 111 plane with two adjacent vacancies. The spatial distribution of conduction is quite different near each vacancy. One can see that the reduction is more pronounced near one of the vacancies. Figure 5f shows the distribution of SPC from the grid closest to the center of the two adjacent vacancies along different directions on this plane. From Fig. 5f, we see that the distribution is highly anisotropic. The recovery length in the direction pointing towards left (blue colored line in Fig. 5c) with (θ, ϕ = 315°, 90°) in Fig. 5 is $\approx$ 7.0 Å. The length pointing downwards with (θ, ϕ = 45°, 145°) in Fig. 5c is $\approx$ 6.1 Å. Along the directions shown by the lines on the right side in Fig. 5e (yellow and green lines), the the recovery length is $\approx$ 5.6 Å.

From the preceding discussion, it is apparent that the spatial distribution of conduction due to single and di-vacancies is quite different, and varies with the crystallographic directions. The degree of anisotropy is higher for the di-vacancy relative to the single vacancy. The recovery length for the single vacancy is up to $\approx$ 6.0 Å and for the di-vacancy is $\approx$ 8.0 Å. The recovery lengths for these studied vacancies are close to the decay length of the density matrix in Al [43].

C. Conduction near grain boundaries

In this section, we briefly discuss on spatial distribution of conduction in aluminum model with GBs. As already described in Sec. II B , we chose two symmetric tilt grain boundaries models, namely Σ5 {-3 1 0} $\langle$ 1 0 0 $\rangle$ and Σ13 {0 -2 3} $\langle$ 1 0 0 $\rangle$. For simplicity, we name these Σ5 and Σ13. For both GB models, we computed SPC in the vicinity of the middle grain (up to $\approx$ 9.0 Å). Figure 6 displays the SPC as 2D color-map projected on xz plane (i.e. 010 plane) along a layer of Al atoms for both GB models. The left and the right subplots correspond to Σ5 and Σ13 respectively. In both subplots, the inverted rainbow color-maps represent the magnitude of SPC values where lower and higher values are shown by red and violet color respectively. It is apparent that the conduction is reduced at the GB, and the effect decays on moving away normal on either sides from the GB. For Σ5 (left subplot in Fig. 6), the conduction mostly recovers at $\approx$ 8.0 Å. On the other hand, the length for Σ13 is close to $\approx$ 6.0 Å, and is shorter compared with Σ5. The recovery length however cannot be generalized from these two symmetric boundaries because many types of grain boundaries exist in metals. From Fig. 6, we see that the distribution pattern of the conduction is unique to the particular grain boundary. In both GBs, most reduction occurs at the empty regions that lie at grain boundaries. One way of improving conductivity

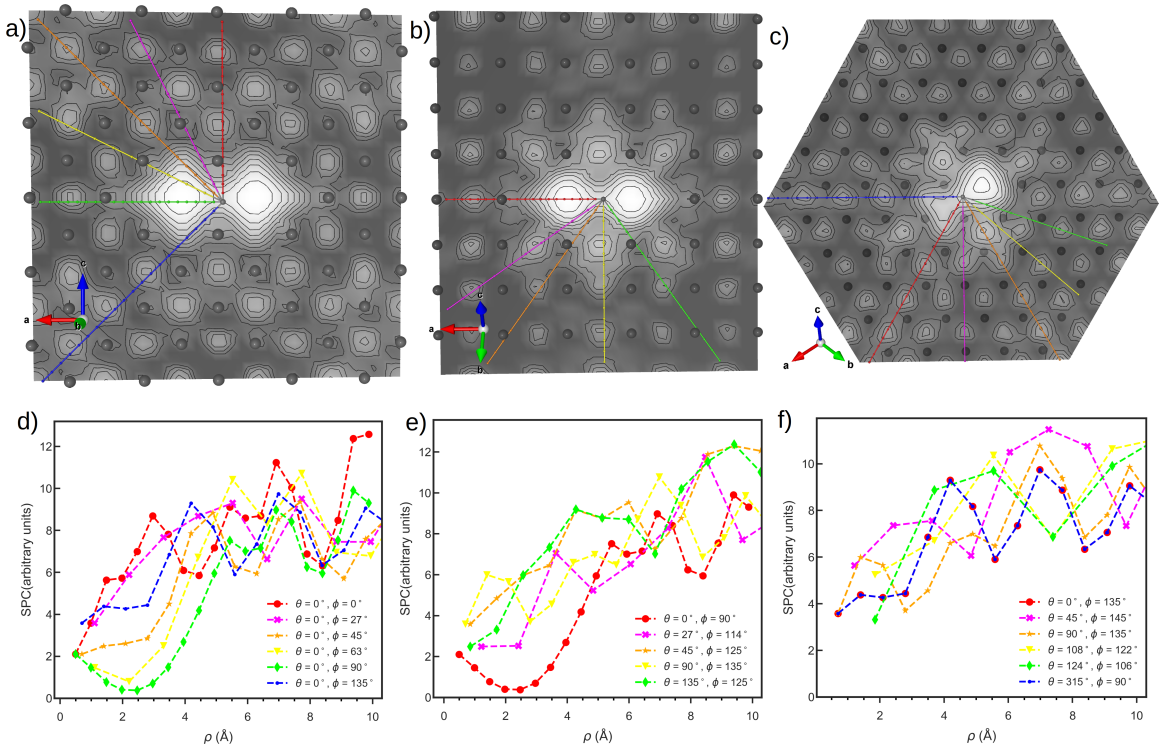

Figure 5. a), b), c): Conductivity projected on grids closest to crystallographic planes 010, 011 and 111 containing the di-vacancies as a 2D gray-scale plot. The magnitude of SPC increases from white to black. The lines with small spheres are just for guide to an eye representing different directions from the vacancy. d), e), f): Variation of conductivity with distance from the grid closest to the center joining two vacancies along different directions on planes 010, 011 and 111 respectively. Colors of legends in d), e), f) match with the lines shown in a), b), c) respectively.

in real metals is by reducing the scattering sites that are abundant at the grain boundaries. Experiments have been done by interfacing Graphene with metals like Al/Cu, and these composites have shown promising enhancement of the conductivity [44, 45].

IV. CONCLUSIONS

In this paper, we utilized the Kubo Greenwood formula to simulate temperature dependence of conductivity in aluminum and obtained results in close accord with the Bloch Grüneisen formula. We showed that the KGF captures T-dependence down to 50 K. We briefly reviewed a method to project conductivity onto a real-space grid, and applied it to study spatial distribution of conduction in aluminum with thermal disorder and lattice defects. We investigated the effect of conduction in the proximity of single and di-vacancies that form prototypes for point defects in the crystal. We computed the range and anisotropy of conduction reduction. The reduction due to di-vacancies is shown to involve longer length scale. We also presented two examples of grain boundaries that are symmetrically tilted. We found that the conduction in such models is reduced at the GB, and the effect decays in a complex way with distance from the GB.

V. ACKNOWLEDGMENT

The authors thank the Hydro-Innovation and Technology Americas for supporting this work under research agreement number 21043 35528. The authors also acknowledge Extreme Science and Engineering Discovery Environment (XSEDE), supported by NSF grant number ACI-15485562 at the Pittsburgh Supercomputer Centers for providing computational resources under allocation DMR-190008P. Pacific Northwest National Laboratory is operated by the Battelle Memorial Institute for the United States Department of Energy under contract DE-AC06-76LO1830. The authors thank Dr. Ronald Cappelletti for helpful discussions.

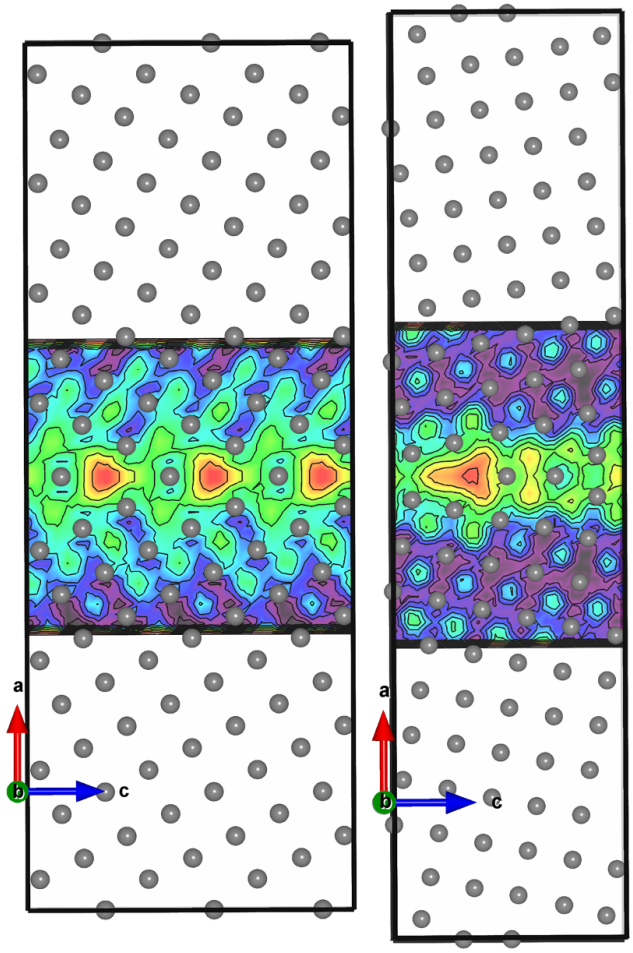

Figure 6. 2D plot of SPC projected on a layer of atoms on 010 plane in the vicinity of the middle grain boundary for two different grain boundary models. Left: Σ5 {-3 1 0} ⟨ 1 0 0 ⟩ and Right: Σ13 {0 2 -3} ⟨ 1 0 0 ⟩. The inverted rainbow colors (ROYGBIV) in both sub-plots represent the magnitude of SPC values with red color corresponding the small values and violet representing the larger values.

[1] L. Boltzmann, "Further studies on the thermal equilibrium of gas molecules," in *The Kinetic Theory of Gases* (1872) pp. 262–349.

[2] E. Lifshitz and L. P. Pitaevskii, *Course of Theoretical Physics Volume 10* (Butterworth-Heinemann, 1981).

[3] A. Sommerfeld, Naturwissenschaften **15**, 825 (1927).

[4] W. V. Houston, Zeitschrift für Physik **48**, 449 (1928).

[5] J. Frenkel and N. Mirolubow, Zeitschrift für Physik **49**, 885 (1928).

[6] F. Bloch, Zeitschrift fr Physik **52**, 555 (1929).

[7] J. M. Ziman and M. H. L. Pryce, Proceedings of the Royal Society of London. Series A. Mathematical and Physical Sciences **226**, 436 (1954).

[8] R. Kubo, J. Phys. Soc. Jpn. **12**, 570 (1957).

[9] A. Einstein, Annalen der Physik **322**, 549 (1905), https://onlinelibrary.wiley.com/doi/pdf/10.1002/andp.19053220806.

[10] A. L. Fetter and J. D. Walecka, *Quantum Theory of Many-Particle Systems* (McGraw-Hill Book Company, New York, 1971).

[11] G. D. Mahan, *Many Particle Physics* (Plenum, New York, 1981).

[12] M. J. Stott and E. Zaremba, Phys. Rev. A **21**, 12 (1980).

[13] W. Yang, Phys. Rev. A **38**, 5512 (1988).

[14] P. B. Allen and J. Q. Broughton, The Journal of Physical Chemistry **91**, 4964 (1987).

[15] T. A. Abtew, M. Zhang, and D. A. Drabold, Phys. Rev. B **76**, 045212 (2007).

[16] S. Lowitzer, D. Ködderitzsch, H. Ebert, and J. B. Staunton, Phys. Rev. B **79**, 115109 (2009).

[17] V. c. v. Vlček, N. de Koker, and G. Steinle-Neumann, Phys. Rev. B **85**, 184201 (2012).

[18] D. Knyazev and P. Levashov, Computational Materials Science **79**, 817 (2013).

[19] L. Caldern, V. Karasiev, and S. Trickey, Computer Physics Communications **221**, 118 (2017).

[20] F. Bloch, Zeitschrift fr Physik **59**, 208 (1930).

[21] Y. Mishin, M. J. Mehl, D. A. Papaconstantopoulos, A. F. Voter, and J. D. Kress, Phys. Rev. B **63**, 224106 (2001).

[22] R. C. Munoz and C. Arenas, Applied Physics Reviews **4**, 011102 (2017).

[23] K. Prasai, K. N. Subedi, K. Ferris, P. Biswas, and D. A. Drabold, physica status solidi (RRL) Rapid Research Letters **12**, 1800238 (2018).

[24] K. N. Subedi, K. Prasai, M. N. Kozicki, and D. A. Drabold, Phys. Rev. Materials **3**, 065605 (2019).

[25] R. Thapa, B. Bhattarai, M. N. Kozicki, K. N. Subedi, and D. A. Drabold, Phys. Rev. Materials **4**, 064603 (2020).

[26] K. N. Subedi, K. Prasai, and D. A. Drabold, "Modeling of glasses: Electronic conduction mechanisms in $GeSe_3$:Ag and Al_2O_3:Cu," in *The World Scientific Reference of Amorphous Materials* (2021) Chap. 3, pp. 79–105.

[27] K. N. Subedi, K. Prasai, and D. A. Drabold, physica status solidi (b) **258**, 2000438 (2021).

[28] S. Nos, The Journal of Chemical Physics **81**, 511 (1984).

[29] N. Shuichi, Progress of Theoretical Physics Supplement **103**, 1 (1991).

[30] D. M. Bylander and L. Kleinman, Phys. Rev. B **46**, 13756 (1992).

[31] V. Randle, *The Role of the Coincidence Site Lattice in Grain Boundary Engineering* (Woodhead Publishing Limited, Cambridge, UK, 1997).

[32] M. A. Tschopp, S. P. Coleman, and D. L. Mcdowell, Integrating Materials and Manufacturing Innovation **4**, 176 (2015).

[33] Y. Mishin, D. Farkas, M. J. Mehl, and D. A. Papaconstantopoulos, Phys. Rev. B **59**, 3393 (1999).

[34] G. Kresse and J. Hafner, Phys. Rev. B **47**, 558 (1993).

[35] G. Kresse and D. Joubert, Phys. Rev. B **59**, 1758 (1999).

[36] J. P. Perdew, K. Burke, and M. Ernzerhof, Phys. Rev. Lett. **77**, 3865 (1996).

[37] D. A. Greenwood, Proceedings of the Physical Society **71**, 585 (1958).

[38] R. M. Feenstra and M. Widom, `www.andrew.cmu.edu/user/feenstra/wavetrans` (2012).

[39] P. Bulanchuk, Computer Physics Communications **261**, 107714 (2021).

[40] C. M. Van Vliet, *Equilibrium and Non-Equilibrium Statistical Mechanics* (WORLD SCIENTIFIC, Singapore, 2008).

[41] J. M. Ziman, *Electrons and Phonons: The Theory of Transport Phenomena in Solids*, Oxford Classic Texts in the Physical Sciences (Oxford University Press, USA, 1960).

[42] A. Chowdhury and S. Bhattacharjee, Journal of Physics D: Applied Physics **46**, 435304 (2013).

[43] X. Zhang and D. A. Drabold, Phys. Rev. B **63**, 233109 (2001).

[44] W. Li, D. Li, Q. Fu, and C. Pan, RSC Adv. **5**, 80428 (2015).

[45] M. Cao, Y. Luo, Y. Xie, Z. Tan, G. Fan, Q. Guo, Y. Su, Z. Li, and D.-B. Xiong, Advanced Materials Interfaces **6**, 1900468 (2019).